Available online at www.sciencedirect.com
ScienceDirect
Geochimica et Cosmochimica Acta 71 (2007) 5528–5543
Geochimica et Cosmochimica Acta
www.elsevier.com/locate/gca

FTIR spectroscopy of OH in olivine: A new tool in kimberlite exploration

S. Matveev *, T. Stachel

Department of Earth and Atmospheric Sciences, University of Alberta, 1-26 Earth Sciences Building Edmonton, Alta., Canada T6G 2E3

Received 14 March 2007; accepted in revised form 30 August 2007; available online 14 September 2007

Abstract

Our study of olivines from Canadian kimberlites shows that the application of FTIR spectroscopy significantly improves the reliability of olivine as a kimberlite indicator mineral (KIM). We have developed an algorithm that yields the water concentration and the normalized intensity of the OH IR absorption band at 3572 cm^{-1} from unpolished olivine grains of unknown thickness. For 80% of kimberlitic olivines these two parameters are significantly higher than those for olivines from non-kimberlitic magmas and consequently, olivines with water concentrations >60 ppm and a strong absorption band at 3572 cm^{-1} can be reliably classified as being kimberlitic.

We have identified two major spectral features in the OH absorption bands of kimberlitic olivines that allow for a more detailed classification: (a) the presence of three types of high-requency OH absorption bands (Group 1A, 1B and 1C) and (b) the proportion of low-frequency OH absorption bands (Group 2) relative to high-frequency bands (Group 1). Comparison of our results with experimental studies suggests that differences within Group 1 OH absorption bands are due to different pressures of crystallization or hydrogenation. The three identified types of Group 1 OH absorption bands approximately correspond to high (P > 2 GPa, Group 1A), moderate (2–1 GPa, Group 1B), and low (<1 GPa, Group 1C) pressures of hydrogenation. Group 2 OH IR absorption bands in olivines with NiO > 3500 ppm are interpreted to reflect olivine–orthopyroxene equilibria and hence are indicative of xenocrystic olivine derived from lherzolitic or harzburgitic mantle sources. Interaction of xenocrystic olivine with hydrous kimberlitic melts with low silica activity likely will cause a gradual increase in Group 1 absorption bands. Therefore, FTIR spectra of olivine can be used to obtain qualitative estimates of the duration of interaction between mantle material and a kimberlitic melt.

In addition to applications in kimberlite and diamond exploration, FTIR spectra of olivine phenocrysts, combined with mineral chemical data, may also provide insights into kimberlite evolution. Our data suggest that in some instances the ascent of kimberlitic magmas could have been interrupted at or near the Moho, followed by olivine crystallization and exsolution of aqueous fluids.

1. INTRODUCTION

During diamond exploration in arctic climates abundant unaltered forsteritic olivine (Fo88-94) is frequently recovered from till samples and, therefore, has the potential to be an excellent kimberlite indicator mineral (KIM). Until now characteristics used to identify kimberlite-derived olivines from mineral concentrate were exclusively based on their chemical composition. Preference was given to olivines with compositions indicative for derivation from depleted lithospheric mantle, i.e. high forsterite (#Mg > 90) and Ni contents (NiO > 0.3 wt%; Griffin et al., 1989). Although xenocrystic olivine derived from disintegrated peridotite xenoliths is very abundant in kimberlites (e.g. Mitchell, 1986; Scott Smith, 1996) such an approach is highly unreliable since it is not possible based on olivine chemistry alone to distinguish xenocrysts from kimberlitic and non-kimberlitic sources. Moreover, in the phenocryst population there is significant

* Corresponding author. Fax: +1 780 4922030.
E-mail address: smatveev@ualberta.ca (S. Matveev).

0016-7037/$ - see front matter © 2007 Elsevier Ltd. All rights reserved.
doi:10.1016/j.gca.2007.08.016

compositional overlap between basaltic and kimberlitic olivines (cf. Mitchell, 1986; Bell et al., 2003b; Karner et al., 2003). Here we will show that FTIR (Fourier Transform Infra Red) spectroscopy may eliminate such ambiguity and allow reliable identification of kimberlitic olivine.

FTIR spectrometry can be used to measure the concentration of hydrogen associated with point defects in the olivine crystal structure (Paterson, 1982; Libowitzky and Rossman, 1997; Bell, 2003a). Since hydrogen is bonded to oxygen in the olivine structure its concentration is commonly expressed as amount of dissolved "water".

Kimberlitic olivines typically contain anomalously high concentrations of water (Miller et al., 1987; Bell et al., 2003b; Matsyuk and Langer, 2004). Experimental data show that the water concentration in olivine increases with increasing water fugacity, i.e. with both pressure and water activity in the surrounding hydrous melt or fluid (Kohlstedt et al., 1996; Matveev et al., 2001). Thus, elevated water concentrations in kimberlitic olivine result from interaction with or crystallization from a hydrous kimberlitic melt at great depth (e.g. within the subcratonic lithospheric mantle). However, extremely high hydrogen diffusion rates in Fe-bearing olivines due to a redox exchange process may cause significant hydrogen loss (Kohlstedt and Mackwell, 1998; Demouchy and Mackwell, 2006). Diffusive hydrogen loss is largely responsible for very low water concentrations in olivines from relatively slowly ascending basaltic magmas (Demouchy et al., 2006; Peslier and Luhr, 2006). At the same time, very rapid ascent of kimberlitic magmas from the deep mantle (Canil and Fedortchouk, 1999; Kelley and Wartho, 2000) will preserve the original water concentrations at least in the core regions of entrained olivine phenocrysts and megacrysts (Bell et al., 2003b). With alteration during weathering and transport generally proceeding from rim to core, it is reasonable to assume that a large proportion of olivines from mineral concentrates collected during kimberlite exploration represent abraded olivine cores or fragments thereof and hence should show strong OH absorption bands. In this case, strong OH absorption bands can be used to quickly and reliably identify a kimberlitic origin of sampled olivines.

The goals of this study are (1) to confirm that high concentrations of water are indeed a characteristic of olivines from Canadian kimberlites, (2) to determine the proportion of olivines with anomalously high water concentrations and (3) to develop an exploration method based on the FTIR spectroscopy of olivine. We demonstrate a straightforward approach to calculate the water concentration in olivine from FTIR spectra only. The proposed method can be used for both polished and unpolished grains. As a first order classification tool it is suggested that high water concentrations correlating with a high IR OH absorption band at 3572 cm^{-1} are the primary characteristic of kimberlitic olivines. We also propose a more detailed classification of OH IR absorbencies based on spectroscopic results from experimental studies (Bai and Kohlstedt, 1993; Kohlstedt et al., 1996; Matveev et al., 2001; Berry et al., 2005). This scheme allows classification of kimberlitic olivines according to their crystallization conditions (broad ranges in pressure and silica activity) and hence may provide insights into the evolution and diamond potential of a specific kimberlite intrusion.

2. SAMPLES

Olivine grains for this study are derived from kimberlites located in the Western, near the edge of the Central, and in the Eastern parts of the Canadian Shield. The various kimberlites differ in eruption age, style of deposition, and dominant kimberlite facies (see also Table 1).

2.1. Lac de Gras kimberlite field, NWT

The first economic diamond deposits in Canada were discovered in 1991 near Lac de Gras on the Central Slave Craton (NWT), (Fipke et al., 1995; Graham et al., 1999). The Lac de Gras kimberlites erupted in the Cretaceous to Tertiary (Eocene) (Heaman et al., 2004, and references therein), forming steep sided and relatively small pipes. The emplacement style differs from South African kimberlites and was classified by Field and Scott Smith (1999) as "Type 3". The rocks are predominantly composed of resedimented volcanoclastic material with an abundant magmatic component and rare mantle xenoliths. Geochemically and petrographically these kimberlites belong to the Group I ("basaltic" kimberlites) of Smith (1983) and Mitchell (1986). Details on the geological setting and rock characteristics may be found in Davis and Kjarsgaard (1997), Brian and Bonner (2003) and Nowicki et al. (2004, and refs. therein).

Studied samples are volcanoclastic and hypabyssal kimberlite recovered from drill core and mine pits. Well

Table 1
Sample localities, sample types and literature references

Sample #	Kimberlite	Sample type	Locality	Reference
A154SA	A154-S	Rock fragment	Lac de Gras, NWT	Graham et al. (1999)
D1 and 2	A154-S	Mineral separate	Lac de Gras, NWT	Graham et al. (1999)
GRZ1	Grizzly	Rock fragment	Lac de Gras, NWT	Nowicki et al. (2004)
SPG-K-1-02	Koala	Mineral separate	Lac de Gras, NWT	Nowicki et al. (2004)
MK01	Misery main	Mineral separate	Lac de Gras, NWT	Nowicki et al. (2004)
MK02	Misery main	Mineral separate	Lac de Gras, NWT	Nowicki et al. (2004)
KIA93	KIA93	Rock fragment	Lac de Gras, NWT	Davis and Kjarsgaard (1997)
FALC1	Fort à la Corne	Mineral separate	Fort à la Corne, Saskatchewan	Berryman et al. (2004)
VIC1	Victor	Mineral separate	Attawapiskat, Ontario	Webb et al. (2004)

consolidated fresh samples of magmatic kimberlite (A154-S pipe at Diavik, KIA93, Grizzly pipe at Ekati) were prepared as polished thin sections. From less consolidated material (Misery and Koala pipes at Ekati) olivines were handpicked, cut and polished for FTIR spectroscopy and EPMA (Electron Probe Micro Analysis). Separated grains ranged from 200 to 1000 μm in diameter and were usually anhedral fragments of larger grains, precluding a morphological classification or recognition of crystal axes.

A number of olivine grains were handpicked from processed kimberlite heavy media concentrate from the A154-S pipe. These grains usually were larger than 2 mm, fresh and un-fractured. As a result of crushing and processing, the recovered olivines were well rounded fragments and their morphology did not carry any information about olivine origin and crystallographic orientation.

2.2. Fort à la Corne kimberlite field, Saskatchewan

The magmatic source for the Cretaceous kimberlites at Fort à la Corne (FALC) is located beneath the buried Archean Saskatchewan micro-craton (Lewry et al., 1994; Chiarenzelli et al., 1996; Canil et al., 2003; Berryman et al., 2004). Kimberlite volcanism is characterized by multiple eruption events which resulted in the formation of wide, shallow craters and tephra cones (Zonneveld et al., 2004). Based on a unique emplacement style, Field and Scott Smith (1999) assigned the FALC kimberlites to a specific Prairie type of diatreme (“Type 2”). Unlike Lac de Gras, drilling showed that FALC kimberlites are dominated by pyroclastic material with abundant fresh olivine macrocrysts.

Studied olivines were made available as mineral separates. The grains were anhedral and ranged in size from 0.2 to 1.5 mm.

2.3. Victor kimberlite, Ontario

The Victor pipe is the largest kimberlite intrusion in the Attawapiskat field (discovered in 1988). During the Jurassic, the Attawapiskat kimberlites intruded the Superior Craton and overlying Paleozoic carbonates. While the pipe shape is similar to the Lac De Gras kimberlites, the dominating rock types are pyroclastics deposits, with both diatreme facies (tuffisitic breccias) and hypabyssal (magmatic) kimberlite being absent. In this respect they resemble kimberlites from FALC (Webb et al., 2004). The complex geology of the Victor pipe suggests multiple stages of kimberlite emplacement, a detailed description is given in Webb et al. (2004).

Olivine grains from the Victor kimberlite were supplied as a mineral separate. The grains were fresh, commonly between 1 and 4 mm in diameter, smooth and anhedral.

3. ANALYTICAL PROCEDURES

3.1. Sample preparation

Rock fragments and individual olivine grains were cut and polished on both sides to produce 100–400 μm thick platelets. For EPMA analysis, the samples were glued on glass slides. To permit FTIR analyses in transmitted mode, rock sections were separated from their glass holders through immersion into acetone. FTIR analyses were also performed on unpolished olivine fragments typically less than 0.5 mm in diameter.

3.2. Electron probe microanalysis

The chemical composition of olivine grains was measured using a JEOL8900 electron microprobe at the University of Alberta, operated at 20 kV accelerating voltage and 100 nA probe current. The beam diameter was set to 5 μm. Count times for major elements (Fe, Mg, Si) were 20 s on peak and 10 s (on each side) for background measurements. For trace elements (Ti, Ni, Ca, Mn, Co, Na) both peak and background times were 40–100 s. For calibration a set of microbeam standards (natural minerals) from the Smithsonian Institution were utilized (Jarosewich, 2002). Data reduction was performed using the $\Phi(\rho Z)$ oxide correction of Armstrong (1995). For trace elements, detection limits (DL) were better than 60 wt ppm. For major elements, Ca and Ni analytical accuracy was verified using secondary standards (San Carlos olivine standards of Köhler and Brey (1990) and Jarosewich (2002). The instrument calibration was deemed successful when the composition of secondary standards was reproduced within the error margins defined by the counting statistics.

3.3. FTIR spectroscopy

Samples were analyzed with a Continuum infrared microscope attached to the Thermo Nicolet Nexus 470 FTIR Spectrometer at the De Beers Laboratory for Diamond Research (University of Alberta). During analysis the IR microscope and bench were continuously flushed with dried air to eliminate spectral noise at 3600 cm^{-1} caused by water vapor in the laboratory air, thereby enhancing the quality of the FTIR spectra and lowering the H_2O detection limit. All measurements were performed in transmitted mode with a beam (aperture) size of 70–100 μm and 60–200 scans were acquired with a spectral resolution 4 cm^{-1}.

Measurements were performed using an unpolarized IR beam providing a stronger signal that also is less dependent on the direction of the incident IR beam relative to the olivine crystal structure. However, partial polarization of the nominally unpolarized IR radiation in the optics of the IR microscope may cause significant deviations from the Beer–Lambert law, and thus hamper quantitative measurements (e.g. Libowitzky and Rossman, 1996; Mosenfelder et al., 2006). Below we evaluate the effect of partial polarization on the 2nd order silica overtone bands (1625–2150 cm^{-1}) and OH absorption bands (3085–3660 cm^{-1}) and demonstrate that the precision and accuracy of quantitative measurements performed with unpolarized IR light are sufficient for applications such as kimberlite exploration.

3.3.1. Effect of partial polarization of the IR beam

The effect of partial polarization was studied on kimberlitic olivines MK01-30 and MK01-33 polished close to

(0 1 0) and (0 0 1) crystal planes, respectively. Each grain was measured at least 10 times with 60 scans acquired per measurement. Before each measurement the olivine grains were rotated by 45 ° in the plane normal to the direction of the incident IR beam. We assumed that any change in IR absorbance with grain rotation is related to partial polarization of the IR beam.

Measured spectra are presented in Fig. 1. The effect of partial beam polarization is best seen in the 2nd order silica overtone range of the measured FTIR spectra: for a beam parallel to [0 1 0] the peaks at 1676, 2023 and 1912 cm^{-1} (including a minor peak on the shoulder located at 1890 cm^{-1}) are changing their intensity with rotation. For a beam parallel to [0 0 1] intensity variations are noticed for bands located at 2023, 1902 and 1763 cm^{-1}. At the same time positions and relative intensities of the OH IR absorption bands largely remain the same.

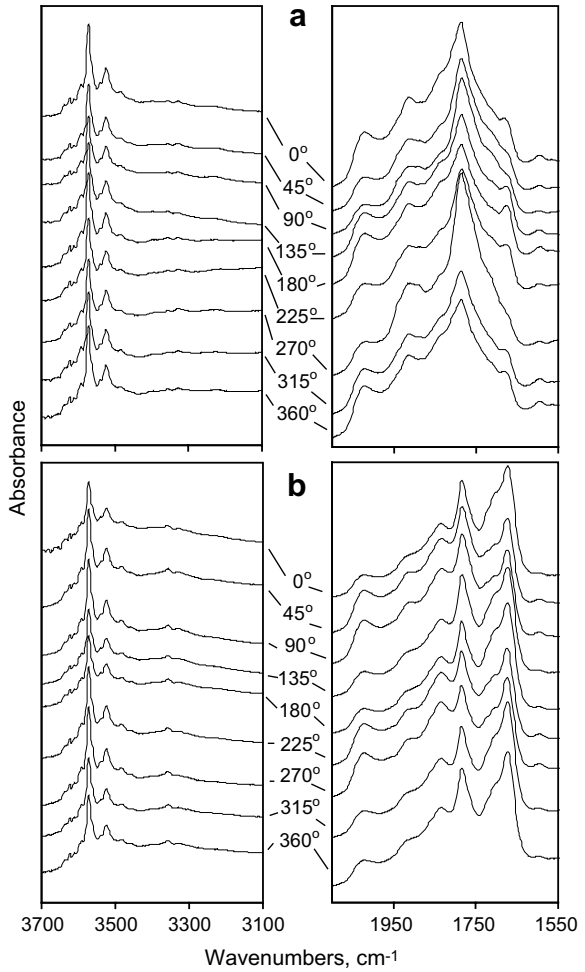

Fig. 1. Effect of partial IR beam polarization during passage through the microscope optics. FTIR spectra measured on samples MK01-30 (a) and MK01-33 (b) polished parallel to (0 1 0) and (0 0 1), respectively. The IR beam was incident normal to the polished plates. As indicated in the diagrams, after each measurement the sample stage was rotated by 45°. Spectra are stacked for clarity.

Absorbance variations can also relate to changes in the overall FTIR spectrum. Integrated absorbencies of the second order Si–O overtone ($A_{\text{int, Si–O overtone}}$) measured at 0 (initial) and 270° grain positions are 15% higher than the average of all measurements (Fig. 1). Similar variability was observed for the integrated OH absorbencies ($A_{\text{int, OH}}$) calculated from the same FTIR spectra (Fig. 2). However, in this case two measurements in identical positions (0° and 360° positions) yielded values different by 15 relative percent and hence the observed variations are not related to partial polarization but reflect analytical uncertainties and/or instrumental drift.

In spite of the above mentioned factors, for all of the polished grains measured $A_{\text{int, Si–O overtone}}$ correlates well with sample thicknesses (t) (Fig. 3). The trend remains linear to at least 400 μm sample thickness and for samples analyzed with an IR beam parallel to [0 1 0] results in following regression:

$$A_{\text{int, Si–O overtone}} = 0.6366t \quad (1)$$

Thus, with an approximate uncertainty of ±15% through data scatter, Beer–Lambert's law is obeyed and unpolarized IR radiation may be used to calculate water concentrations. This is generally consistent with the results of Libowitzky and Rossman (1996) for samples less than 1 mm in thickness (see their Fig. 3).

Note that errors introduced due to changes in overall absorbance (Fig. 2) are probably largely compensated if sample thickness is determined from $A_{\text{int, Si–O}}$ using (1) rather than measured independently. To completely eliminate the effect of partial beam polarization and to enhance

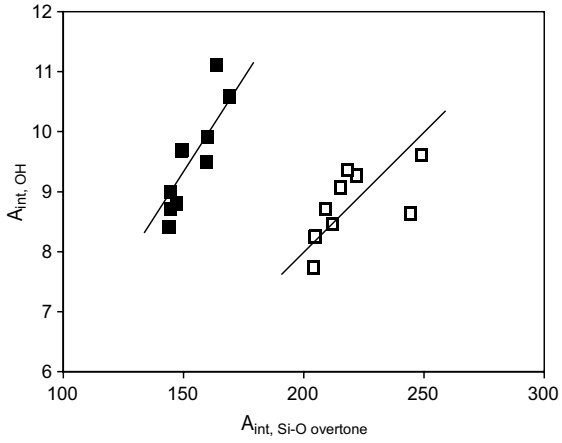

Fig. 2. Correlation between integrated absorbencies in the OH (from 3085–3656 cm^{-1}) and the 2nd order Si–O overtone absorption regions (from 1625–2150 cm^{-1}), as calculated from the spectra shown in Fig. 1. Filled and open symbols represent data for MK01-30 and MK01-33, respectively. Solid lines are linear data regressions forced through 0. A notable correlation of the integrated intensities of the two absorption regions (which are entirely different in nature) suggests that absorbencies may simultaneously increase or decrease for the entire spectrum. This implies that changes in peak intensities are not only due to partial beam polarization, but strongly depend on the stability of the signal registered by the FTIR spectrometer.

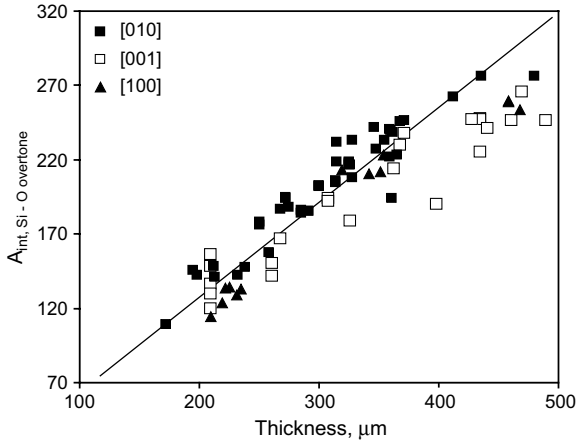

Fig. 3. Integrated absorbencies of the 2nd order SiO overtone as a function of thickness of the polished olivine grains. The linear regression derived here is used in Eq. (1) to calculate the thickness of unpolished grains using their 2nd order SiO overtone. Fig. 2 implies that this use of method to estimate sample "thickness" improves the precision of calculated water concentrations for both polished and unpolished grains, as it automatically eliminates instrumental instability.

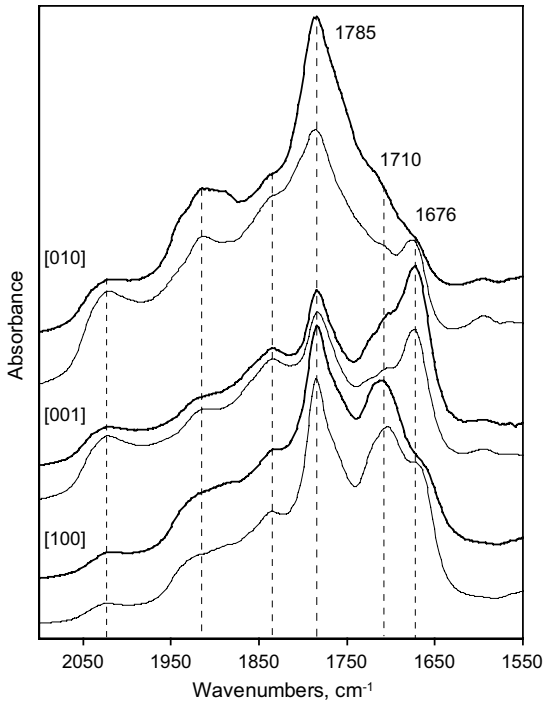

Fig. 4. Characteristic IR absorbencies of the 2nd order Si–O overtone, measured with an IR beam parallel to each of the three principal olivine crystallographic directions. Differences in absorbencies measured at the same beam direction are attributed to partial beam polarization through the optics of the FTIR microscope. Spectra are stacked for clarity.

analytical precision, absorption spectra obtained for the same grain at different stage positions may be averaged. For example, processing of the averaged data shown in Fig. 1 would yield precise water concentrations for MK01-30 and MK01-33.

3.3.2. Calculation of water concentrations in olivine

Primary requirements for the application of spectroscopic analyses in mineral exploration are (1) reproducibility of the data and (2) automation of data processing. We therefore developed an algorithm that could be implemented as a macro, eliminating the necessity for any additional measurements (sample thickness, orientation). The sample thickness is determined using regression (1). The beam orientation is evaluated using the spectrum of the 2nd order Si–O overtone (Fig. 4, Jamtveit et al., 2001; Matveev et al., 2005).

Although the determination of absolute water concentrations may not play a critical role for kimberlite exploration, where consistent relative measurements likely will suffice, our procedure to calculate water concentration was developed with the goal to yield accurate values that are comparable to results obtained employing widely used calibrations (Paterson, 1982; Libowitzky and Rossman, 1997; and Bell, 2003a).

The calculation procedure is based on formulae from Paterson (1982). This calibration presumes a wavelength dependency of the molar absorption coefficient. Such a dependency was confirmed for high energy OH absorption bands (3700 to 3200 cm^{-1}) for a variety of minerals (Skogby and Rossman, 1991; Bell et al., 1995; Libowitzky and Rossman, 1997) and thus is assumed to be applicable to olivine as well. Libowitzky and Rossman (1997) emphasized the importance of using integrated intensities for the calculation of water concentrations and molar absorption coefficient corrections. To comply with this requirement and to compensate for the broad wavenumber range of OH absorption in olivine, the FTIR spectra were divided into three parts, corresponding to three groups of OH IR absorption bands (see Fig. 5; Bai and Kohlstedt, 1993; Matveev et al., 2001; Lemaire et al., 2004). The wavenumber positions for the bounds of each group were carefully selected based on more than 100 FTIR spectra. During posi-

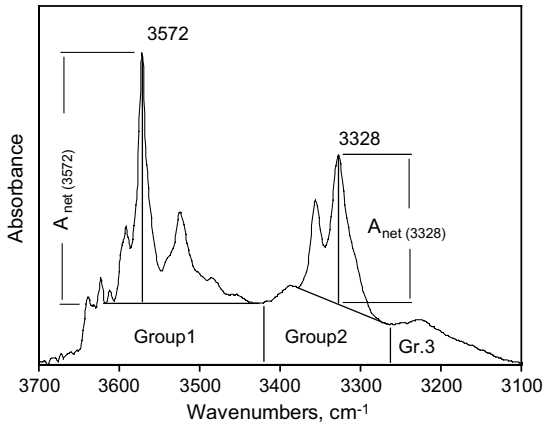

Fig. 5. The division of the OH absorption region of olivine between 3700 and 3100 cm^{-1} into Groups 1, 2 and 3. For further discussion see text.

tioning of these limits particular care was taken to avoid unrelated IR absorption peaks and their shoulders, including peaks due to olivine alteration. The wavenumber ranges for the three groups were defined as: (1) 3415–3653 cm^{-1}; (2) 3265–3415 cm^{-1} and (3) 3099–3265 cm^{-1}. The wavelength dependency of the molar absorption coefficient for each group was compensated for separately similar to the procedure outlined in Libowitzky and Rossman (1997) their Fig. 1. Considering the variability of OH IR absorption bands in kimberlitic olivines, calculation of weighed mean wavenumbers for every group in every spectrum would not be feasible. Instead, for each group of bands the wavenumber of its strongest absorption peak was used as its nominal position (ν^*), i.e. 3572, 3328, and 3228 cm^{-1} for Groups 1, 2 and 3, respectively. Each segment of the OH absorption spectrum was integrated using a linear baseline set at 3130 and 3755 cm^{-1} and divided by $3780 - \nu^*$ (Paterson, 1982; Libowitzky and Rossman, 1997).

The latest calibration for olivine of Bell (2003a) yields water concentrations that are 3.5 times higher than values obtained via the calibration of Paterson (1982) for an unpolarized IR beam. To make our results consistent with Bell (2003a) we introduced 3.5 as an additional coefficient and the resulting expression is:

$$C_{H_2O}\,(\mathrm{wt\%}) = D \times 3.5 \times K \times \left(\frac{A_{\mathrm{int}}(3415-3653)}{3780-3572} + \frac{A_{\mathrm{int}}(3265-3415)}{3780-3328} + \frac{A_{\mathrm{int}}(3099-3265)}{3780-3228}\right), \quad (2)$$

where D is a coefficient used to normalize measured absorbencies to 1 cm sample thickness. $D = \frac{10{,}000}{t}$, with t being calculated from $A_{\mathrm{int,\ Si\text{–}O\ overtone}}$ using (1). K is a pre-integral coefficient calculated using the molar absorption coefficient from Paterson (1982) and includes all the transformations necessary to yield concentrations of water in wt%. The expanded version of K is:

$$K = \frac{1000 \times 0.5 \times M(H_2O)}{150 \times \gamma \times \rho(\mathrm{ol})} = 36.37 \quad (3)$$

Here, $M(H_2O) = 18$ is the molecular weight of water, $\rho(\mathrm{ol}) = 3.3\ \mathrm{g/cm^3}$ is density of forsteritic olivine, and $\gamma = 0.5$ is the orientation factor (Mackwell and Kohlstedt, 1990).

Our algorithm follows existing quantitative calibrations and, therefore, for spectra measured at a beam direction parallel to [0 1 0], will yield H_2O concentrations with comparable accuracy. For other beam orientations concentrations will be systematically underestimated, but such spectra may still be used to identify kimberlitic olivines.

Analytical precision is determined by (1) effects of partial polarization (see Section 3.3.1); (2) spectral noise and (3) nonlinearity of the spectral baseline. For olivines with relatively high concentrations of water (>40 ppm), precision is primarily controlled by effects due to partial polarization and estimated to be better than ±15% relative (Fig. 3). Consequently, analytical precision can be improved by averaging results of a few measurements performed at different stage positions (see Section 3.3.1). Spectral noise depends on the analytical setup of the particular laboratory. Purging of the spectrometer and the IR optics with dried air insures minimal spectral noise and estimated detection limits for our olivine analyses were ~1 wt ppm H_2O. Nonlinearity of the baseline may significantly contribute to the error during analysis of the water-poor olivines. Thus, for measurements of low water concentrations the algorithm would need to be amended. However, quantitative FTIR measurements of water concentrations in water-poor olivine grains is beyond the scope of this study.

4. RESULTS AND DISCUSSION

4.1. FTIR spectra of kimberlitic olivines

FTIR spectra of kimberlitic olivines are quite diverse and it is impossible to isolate a certain type of spectrum characteristic of a kimberlitic origin. Even within a single thin section of magmatic kimberlite, olivines show practically every OH absorption band previously measured in natural or in experimentally annealed, Fe-bearing forsteritic olivines (Fo84–Fo96) (e.g. Miller et al., 1987; Bai and Kohlstedt, 1993; Kohlstedt et al., 1996; Matveev et al., 2001; Bell et al., 2003b; Lemaire et al., 2004; Matsyuk and Langer, 2004; Matveev et al., 2005). Fig. 5 illustrates major spectral characteristics that will be used below to describe the observed range in OH IR absorption bands of kimberlitic olivines.

Below, in order to categorize the spectroscopic information, FTIR spectra are divided into three major types (a, b and c, see Fig. 6) based on the fine structure of Group 1 absorption bands. Including two additional parameters—the relative proportion of Group 2 bands and the water concentration—allows describing every spectrum measured on kimberlitic olivines. This classification scheme is designed to rapidly categorize a statistically representative

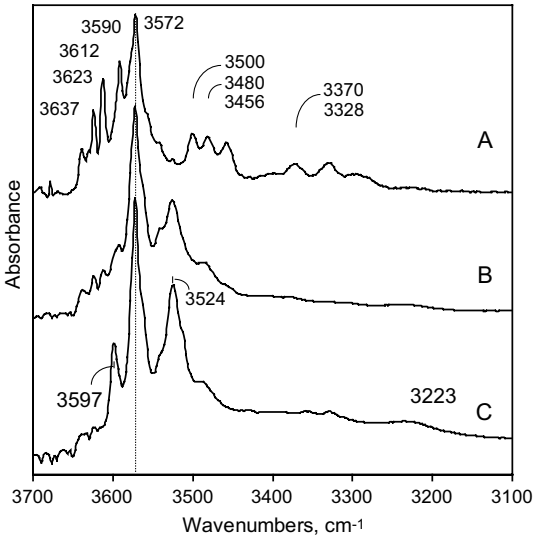

Fig. 6. The three types of Group 1 IR OH absorption bands, corresponding to different pressures of crystallization/hydrogenation (see text). Intensities of the 3572 cm^{-1} absorption peak are reduced to approximately similar values for easy comparison and spectra are stacked for clarity.

number of olivine grains from kimberlite or mineral concentrate samples in order to characterize a kimberlite intrusion. The spectral characteristics can be interpreted with respect to the conditions of olivine crystallization/re-equilibration and thus provide insights into the evolution of a specific batch of kimberlite magma. Lastly we define primary characteristics of kimberlitic olivines for use in the examination of indicator mineral samples in kimberlite exploration.

4.1.1. Group 1 OH IR bands

Practically every spectrum measured on the OH-rich olivines typical for kimberlites shows a strong peak at 3572 cm^{-1}. The positions and intensities of other peaks present are used to isolate the three major types of Group 1 bands shown in Fig. 6.

Group 1A spectra include multiple absorption bands at wavenumbers above 3572 cm^{-1} (at 3590, 3612, 3623 and 3637 cm^{-1}) and at lower frequencies (3328, 3370, 3456, 3480 and 3500 cm^{-1}). Such spectra are similar to those previously reported for olivines annealed in high pressure ($P > 2$ GPa) hydrogenation experiments (Kohlstedt et al., 1996; Matveev et al., 2001; Mosenfelder et al., 2006). For kimberlitic olivines such spectra may also imply hydrogenation at high pressures. The low frequency OH IR absorption band at 3328 cm^{-1}overlaps with one of the Group 2 bands. Despite this overlap, low frequency bands in Group 1A spectra result from different defects than Group 2 bands (e.g. Matveev et al., 2001; Berry et al., 2007). Therefore, low-frequency bands in this overlap region may be confidently assigned to either Group 1A or Group 2 based on other bands observed in the spectrum and the absorption band at 3328 cm^{-1} is only allocated to Group 1A if associated with other low frequency bands of this group.

Group 1C spectra, besides the main peak at 3572 cm^{-1}, show only two strong absorption peaks located at 3524 and 3597 cm^{-1}. Similar spectra were measured in olivine phenocrysts from basaltic melts (Matveev et al., 2005) and peridotitic olivines experimentally annealed at relatively low pressures (<1 GPa) (Bai and Kohlstedt, 1993; Zhao et al., 2004). Such spectra could be characteristic of olivine crystallization/hydrogenation at low pressures.

Group 1B is an intermediate type. The FTIR spectra have both the high-frequency OH absorption bands characteristic of type A and the prominent absorption peak at 3524 cm^{-1} band indicative of type C. Hydrogenation of olivines with such spectra likely occurred at intermediate pressures of ~1–2 GPa.

Very high concentrations of Ti in olivine can stabilize the peak at 3524 cm^{-1} to higher pressures (Berry et al., 2007). Unfortunately, this effect was not yet studied for the range of Ti concentrations commonly observed in kimberlitic olivines. In this study we assume that Ti concentrations in kimberlitic olivines are too low (Table 2) to significantly alter the primary control that pressure exerts on the position of OH absorption bands.

4.1.2. Group 2 absorption bands and the $A_{net\ ratio}$

In over 40% of olivines studied, hydroxyl absorbs IR radiation at 3355 and 3328 cm^{-1} (Fig. 7). After Bai and Kohlstedt (1993) these bands are commonly referred to as to Group 2 OH absorption bands and their origin is extensively debated in literature (e.g. Bai and Kohlstedt, 1993; Matveev et al., 2001; Matsyuk and Langer, 2004; Berry et al., 2005, 2007; Grant et al., 2007a). The relative intensity of Group 2 bands is potentially an important exploration parameter. Thus, below we evaluate the available information to define conditions that may lead to the development of this type of hydrous defects in the olivine structure.

The latest experimental results show that Group 2 OH bands are associated with the presence of trivalent cations (e.g. Al^{3+}, Cr^{3+}, Fe^{3+}) in the olivine crystal structure (Berry et al., 2005, 2007; Grant et al., 2007b). Consistently, these bands were never observed in FTIR spectra of synthetic pure Mg_2SiO_4 forsterite (Lemaire et al., 2004; Berry et al., 2007; Smyth et al., 2006). Available experimental studies, however, diverge strongly in the interpretation of the conditions that lead to the formation of these hydrous defects. Experimentally annealed, natural Fe-bearing olivines exclusively showed Group 2 OH IR absorption bands when in equilibrium with orthopyroxene (high $aSiO_2$). These results were obtained at relatively oxidizing conditions ($fO_2 \geqslant$ NNO, where NNO denotes the Ni–bunsenite oxygen fugacity (fO_2) buffer) and pressures of 1.6–2 GPa (Matveev, 1997; Matveev et al., 2001; Berry et al., 2007). At similarly oxidizing conditions, Group 2 bands were not observed in Fe-bearing olivines at low $aSiO_2$ (equilibrium with magnesiowüstite). Thus, Matveev et al. (2001) suggested that high $aSiO_2$ is necessary to produce the corresponding hydrous defects. At the same time, in a number of experiments conducted at similar conditions at somewhat higher (e.g. Kohlstedt et al., 1996; Mosenfelder et al., 2006) or lower pressures (e.g. Kohlstedt and Mackwell, 1998) no Group 2 bands were observed in olivine. In the experiments of Zhao et al. (2004) olivine annealed at high $aSiO_2$ and at fO_2 buffered at NNO showed FTIR spectra in which the intensity of Group 2 bands increased with increasing temperature. The conflicting experimental results may suggest that the formation of hydrous defects corresponding to Group 2 OH absorption bands is very sensitive to equilibration conditions. Defect formation may also depend on the mechanism of hydrogen incorporation (Demouchy and Mackwell, 2006) and attainment of complete crystal–chemical equilibrium (Matveev et al., 2001).

Although in experimental run products Group 2 OH absorption bands are apparently less common than Group 1 bands, they are frequently observed in natural olivines formed over a wide range of pressures ranging from the relatively shallow crystallization conditions of basaltic phenocrysts to the high pressure conditions of the garnet peridotite stability field (e.g. Matveev et al., 2005, 2006; Demouchy et al., 2006; Grant et al., 2007a). Thus, natural observations are not in line with a proposed pressure effect on Group 2 OH bands (Mosenfelder et al., 2006).

Group 2 bands have been observed in natural olivines from different fO_2 environments: in basaltic phenocrysts crystallized at $fO_2 \sim FMQ + 1$ (Portnyagin, 1998; Matveev et al., 2005), in olivines from the spinel peridotites (Grant et al., 2007a), in less oxidized olivines from garnet peridotites (Demouchy et al., 2006), and in reduced olivines from

Table 2
Analytical results

Sample #	Spectrum type	$A_{\text{int ratio}}$	$A^{*}_{\text{net}(3572)}$	SiO_2 (wt%)	FeO (wt%)	MgO (wt%)	TiO_2 (ppm)	Al_2O_3 (ppm)	Cr_2O_3 (ppm)	MnO (ppm)	NiO (ppm)	CaO (ppm)	CoO (ppm)	Na_2O (ppm)	H_2O (ppm)	Total
A154SA 14B	B-0.97	0.97	2.77	40.2	8.4	50. 7	150 ± 32	173 ± 77	430 ± 40	1063 ± 40	3883 ± 55	393 ± 21	363 ± 36	127 ± 30	153	100.0
A154SA 15B	A-0.44	0.44	0.45	40.6	7.3	52. 0			310 ± 45	958 ± 39	3598 ± 71	135 ± 45	303 ± 40		47	100.4
A154SA 16B	A-0.65	0.65	0.39	40.4	8.2	51. 1		67 ± 57	377 ± 38	1080 ± 40	3893 ± 54	417 ± 28	387 ± 61		31	100.4
A154SA 17 3	A-1	1.00	0.45	40.7	6.8	52. 4				893 ± 42	3780 ± 60	66 ± 57	343 ± 30		30	100.5
A154SA 19 1	A-0.54	0.54	0.68	40.6	6.9	52. 3		97 ± 96	330 ± 39	890 ± 38	3473 ± 52	117 ± 32	273 ± 65		66	100.3
A154SA 21 1	B-1	1.00	3.49	40.3	8.4	50. 7	160 ± 52	67 ± 57	257 ± 46	1107 ± 50	3490 ± 53	340 ± 20	273 ± 40	90 ± 22	153	100.0
A154SA 22 2	A-0.94	0.94	0.59	40.3	8.1	50. 9		0	337 ± 35	1050 ± 39	3927 ± 80	430 ± 21	327 ± 40	60 ± 52	94	100.0
A154SA 23 1	B-1	1.00	5.23	40.1	9.4	50. 2	330 ± 31	75 ± 50	230 ± 41	1170 ± 40	3173 ± 63	375 ± 52	360 ± 31	85 ± 28	220	100.3
A154SA 24 1	B-1	1.00	3.16	40.3	8.3	50. 9	155 ± 47	155 ± 64	313 ± 42	1018 ± 40	3778 ± 54	390 ± 20	328 ± 46	115 ± 25	192	100.1
D1-1	C-1	0.65	0.23	40.2	7.7	50. 8				1008 ± 42	3442 ± 74		273 ± 50		5	99.2
D1-2	B-0.89	0.89	2.21	40.1	7.8	50. 8	70 ± 62	80 ± 72	350 ± 38	1023 ± 95	3810 ± 103	320 ± 23	300 ± 55	83 ± 27	150	99.3
D1-3	B-1	1.00	3.16	39.7	9.6	49. 3	193 ± 60	73 ± 63	237 ± 33	1060 ± 65	3260 ± 53	406 ± 20	353 ± 28	120 ± 36	220	99.2
D1-5	B-0.9	0.90	2.61	39.9	8.6	50. 0	100 ± 49	88 ± 44	353 ± 56	1046 ± 37	3763 ± 68	360 ± 27	302 ± 56	103 ± 22	164	99.1
D1-7	B-1	1.00	4.53	40.0	7.7	50. 8	150 ± 44		290 ± 43	890 ± 63	3950 ± 54	223 ± 22	340 ± 74	83 ± 52	252	99.0
D1-9	B-1	1.00	4.47	40.3	11.2	48. 4	251 ± 27		126 ± 40	1420 ± 47	2346 ± 80	348 ± 25	31 8 ± 58		233	100.4
D1-10	B-1	1.00	4.11	39.5	10.2	49. 1	280 ± 33	73 ± 58	160 ± 43	1238 ± 55	2468 ± 49	318 ± 19	351 ± 32	103 ± 22	269	99.3
D1-11	B-1	1.00	4.69	40.2	10.4	49. 0	300 ± 36	66 ± 51	145 ± 45	1246 ± 48	2290 ± 55	346 ± 21	340 ± 44	66 ± 54	260	100.0
D1-12	B-1	1.00	5.93	40.2	10.0	49. 5	301 ± 45	68 ± 53	211 ± 55	1151 ± 56	2700 ± 49	318 ± 22	338 ± 51	65 ± 55	290	100.2
D2-1	B-0.97	0.97	2.59	40.8	6.7	52. 2	70 ± 56		111 ± 44	788 ± 37	3741 ± 54	80 ± 40	261 ± 46		108	100.1
D2-6	B-1	1.00	5.44	40.0	8.9	50. 2	318 ± 39		330 ± 42	1133 ± 61	3316 ± 52	236 ± 52	34 6 ± 73	63 ± 50	292	99.7
D2-7	B-1	1.00	6.34	40.1	8.0	50. 4	308 ± 58	72 ± 70	318 ± 35	1020 ± 40	3644 ± 74	268 ± 40	296 ± 33	88 ± 20	299	99.1
FALC1-1	C-0.97	0.97	3.17	40.5	9.6	50. 1	237 ± 38	227 ± 29	467 ± 32	1047 ± 34	3717 ± 42	670 ± 10	273 ± 55	247 ± 25	206	100.9
FALC1-4	C-0.98	0.98	1.85	39.6	10.5	48. 8	260 ± 25	130 ± 30	317 ± 32	1077 ± 66	3227 ± 45	607 ± 20	340 ± 30	173 ± 37	127	99.4
FALC1-5	C-0.98	0.97	1.63	40.1	9.2	49. 2	190 ± 44	183 ± 60	496 ± 31	1046 ± 41	3807 ± 41	720 ± 7	343 ± 56	176 ± 21	116	99.2
FALC1-7	C-0.95	0.95	1.20	40.6	9.2	49. 9	110 ± 19	180 ± 40	553 ± 30	1023 ± 34	3767 ± 42	757 ± 30	300 ± 75	200 ± 40	103	100.4
FALC1-9	C-0.93	0.93	2.62	40.1	8.5	50. 5	150 ± 21	120 ± 28	540 ± 32	970 ± 34	3810 ± 99	650 ± 10	340 ± 29	186 ± 35	180	99.7
FALC1-11	C-0.78	0.78	2.11	40.4	8.7	50. 7	170 ± 23	197 ± 70	1077 ± 35	1100 ± 34	3750 ± 42	680 ± 17	357 ± 30	270 ± 34	147	100.6
GRZ1-1-2-1	A-1	1.00	2.39	40.5	7.7	50. 5		260 ± 56	175 ± 35	915 ± 31	3685 ± 52	245 ± 21	290 ± 29		135	99.3
GRZ1-1-4-1	A-1	1.00	1.52	40.5	9.3	49. 1		110 ± 24	110 ± 27	1305 ± 35	3835 ± 51	185 ± 49	315 ± 49		78	99.4
GRZ1-1-6-1	AB-1	1.00	2.78	40.3	9.1	49. 5		120 ± 28	120 ± 42	1285 ± 30	3740 ± 56	345 ± 12	335 ± 148	85 ± 21	126	99.5
GRZ1-1-6-2	A-1	1.00	2.60	40.7	7.5	50. 7	145 ± 35		250 ± 42	1040 ± 56	3295 ± 91	185 ± 35	345 ± 30	110 ± 16	127	99.4
GRZ1-2-1-2	A-1	1.00	1.13	41.4	7.5	50. 2		415 ± 148	335 ± 25	940 ± 31	3565 ± 53	220 ± 14	330 ± 85	130 ± 19	72	99.6
GRZ1-2-2	A-1	1.00	3.57	40.2	7.7	50. 6		100 ± 22	270 ± 22	950 ± 31	3640 ± 52	160 ± 9	310 ± 29	0 ± 0	187	99.0
GRZ1-2-4-1	low water	1.00	0.07	40.8	9.0	48. 9	98 ± 23	232 ± 38	535 ± 26	1065 ± 46	3810 ± 52	645 ± 90	345 ± 35	165 ± 22	3	99.3
GRZ1-2-5-1	A-1	1.00	3.91	40.7	7.4	50. 9	142 ± 32		252 ± 26	785 ± 33	3535 ± 53	295 ± 20	285 ± 28	142 ± 55	156	99.5
GRZ1-2-6-1	A-1	1.00	1.34	40.8	6.7	51. 2			160 ± 42	895 ± 35	3565 ± 64	150 ± 28	260 ± 28	80 ± 14	117	99.2
GRZ1-2-8-2	A-1	1.00	2.31	40.5	11.8	48. 5	245 ± 36	275 ± 78	110 ± 26	1365 ± 35	2680 ± 53	355 ± 21	390 ± 141	275 ± 35	122	101.4
GRZ1-2-10-1	B-1	1.00	2.21	40.7	7.7	51. 4	130 ± 26		420 ± 26	966 ± 31	4010 ± 51	423 ± 98	366 ± 30	143 ± 32	105	100.4
KIA93-4	B-1	1.00	2.69	39.9	8.9	50. 1	150 ± 27		246 ± 38	1200 ± 55	3263 ± 60	286 ± 19	313 ± 49	110 ± 19	95	99.5
KIA93-16	C-1	1.00	0.92	40.2	8.9	50. 2	100 ± 23	960 ± 183	260 ± 21	995 ± 63	3695 ± 52	490 ± 42	360 ± 30	365 ± 134	29	100.0

(*continued on next page*)

Table 2. (*continued*)

Sample #	Spectrum type	$A_{\text{int ratio}}$	$A^{*}_{\text{net}(3572)}$	SiO_2 (wt%)	FeO (wt%)	MgO (wt%)	TiO_2 (ppm)	Al_2O_3 (ppm)	Cr_2O_3 (ppm)	MnO (ppm)	NiO (ppm)	CaO (ppm)	CoO (ppm)	Na_2O (ppm)	H_2O (ppm)	Total
KIA93-21	C-1	1.00	0.24	40.3	9.0	49. 6	76 ± 68	106 ± 24	276 ± 37	1020 ± 34	3730 ± 52	426 ± 22	313 ± 61	153 ± 55	1	99.5
MK01-03	B-0.9	0.90	1.24	40.5	8.4	50. 7	103 ± 14	110 ± 21	743 ± 26	1097 ± 27	3803 ± 33	393 ± 8	347 ± 74	233 ± 23	57	100.3
MK01-04	B-0.91	0.91	2.45	40.4	8.6	50. 5	113 ± 15	104 ± 31	560 ± 46	1073 ± 29	3757 ± 37	413 ± 23	320 ± 53	180 ± 22	212	100.1
MK01-05	B-0.92	0.82	2.14	40.6	7.3	51. 5	93 ± 14	113 ± 22	433 ± 26	943 ± 28	3530 ± 66	340 ± 9	283 ± 24	117 ± 17	107	100.0
MK01-06	B-0.96	0.96	2.58	40.4	9.0	50. 3	120 ± 26	147 ± 29	397 ± 22	1060 ± 61	3927 ± 32	397 ± 8	330 ± 24	240 ± 72	184	100.3
MK01-08	B-1	1.00	1.85	40.4	9.4	50. 1	107 ± 14	107 ± 21	187 ± 26	1013 ± 35	3880 ± 78	337 ± 12	350 ± 79	133 ± 19	104	100.5
MK01-12	B-0.63	0.64	1.15	40.5	7.6	51. 3		80 ± 70	373 ± 40	963 ± 28	3707 ± 38	363 ± 8	310 ± 35	113 ± 17	86	100.0
MK01-15	B-0.93	0.98	1.66	40.3	9.3	50. 2	100 ± 14	100 ± 20	247 ± 29	1023 ± 27	3890 ± 32	330 ± 10	347 ± 24	137 ± 19	114	100.4
MK01-16	B-0.92	0.92	3.00	40.5	8.0	50. 9	100 ± 17	110 ± 26	383 ± 27	973 ± 42	3583 ± 49	247 ± 12	297 ± 60	113 ± 21	147	100.0
MK01-20	B-0.86	0.86	2.25	40.4	8.4	50. 7	100 ± 14	143 ± 38	717 ± 31	1043 ± 31	3860 ± 33	393 ± 8	323 ± 24	220 ± 23	92	100.2
MK01-23	B-0.85	0.85	2.92	40.4	9.1	50. 2	110 ± 15	107 ± 21	387 ± 20	1083 ± 32	3700 ± 46	350 ± 10	337 ± 24	90 ± 20	130	100.3
MK01-26	B-1	1.00	2.37	40.3	9.0	50. 3	105 ± 14	110 ± 21	240 ± 42	1030 ± 57	3935 ± 32	300 ± 14	325 ± 24	160 ± 42	155	100.3
MK01-29	B-0.91	0.91	1.70	40.2	8.9	50. 1	93 ± 14	163 ± 61	537 ± 15	1057 ± 32	3807 ± 33	420 ± 10	337 ± 31	203 ± 32	67	99.8
MK01-30	B-0.97	0.97	2.55	40.3	9.0	50. 2	133 ± 15	133 ± 23	417 ± 29	1020 ± 27	3917 ± 74	397 ± 15	320 ± 24	213 ± 45	146	100.1
MK01-31	B-0.83	0.83	1.59	40.2	8.6	50. 5		103 ± 21	360 ± 28	1050 ± 27	3903 ± 32	383 ± 8	333 ± 24	107 ± 21	101	99.9
MK01-32	B-0.90	0.90	0.64	40.1	9.1	50. 0		123 ± 22	403 ± 129	977 ± 38	3897 ± 99	363 ± 49	323 ± 24	147 ± 19	27	99.8
MK01-35	B-1	1.00	2.55	40.2	9.6	49. 7	123 ± 25	130 ± 30	247 ± 12	1117 ± 27	3383 ± 37	353 ± 12	340 ± 24	203 ± 75	178	100.1
MK01-36	B-0.94	0.94	2.04	40.3	8.9	50. 2	97 ± 14	147 ± 24	280 ± 20	1043 ± 27	3943 ± 55	413 ± 8	347 ± 31	183 ± 47	190	100.0
MK02-07	B-0.98	0.98	3.49	40.3	7.3	51. 3			478 ± 16	928 ± 45	3773 ± 42	210 ± 10	268 ± 27	13 3 ± 18	197	99.6
MK02-10	B-0.98	0.98	3.33	40.6	7.3	51. 7	93 ± 17	107 ± 22	387 ± 27	913 ± 32	3483 ± 44	327 ± 10	253 ± 32	150 ± 36	159	100.2
SPG-K-1-02	B-1	1.00	1.40	40.5	7.8	51. 4	320 ± 17		460 ± 32	1046 ± 27	3653 ± 42	230 ± 9	280 ± 36	140 ± 20	61	100.3
VIC1-1-1	A-1	1.00	1.52	39.4	11.3	48. 9	270 ± 26	100 ± 20	163 ± 32	1213 ± 25	2590 ± 61	263 ± 6	383 ± 29	130 ± 10	73	100.1
VIC1-1-2	B-1	1.00	5.16	40.4	7.5	51. 7				1150 ± 99	3380 ± 84		270 ± 27		273	100.1
VIC1-2-1	A-1	1.00	1.64	38.9	11.9	48. 2	303 ± 26	100 ± 22	127 ± 25	1260 ± 35	2160 ± 36	256 ± 6	370 ± 20	183 ± 45	92	99.6
VIC1-3-1	A-1	1.00	1.34	40.6	10.3	49. 0	3 ± 23	160 ± 26	247 ± 57	1083 ± 45	3383 ± 45	380 ± 26	353 ± 29	207 ± 40	79	100.6
VIC1-3-2	B-1	1.00	6.69	40.4	8.5	50. 4	103 ± 18		347 ± 31	957 ± 45	3697 ± 40	287 ± 15	310 ± 46	97 ± 38	365	99.8
VIC1-4-1	C-0.7	0.71	1.12	40.5	10.3	48. 9	273 ± 23	107 ± 22	180 ± 32	1197 ± 40	3013 ± 46	263 ± 32	343 ± 32	150 ± 52	87	100.3
VIC1-4-2	B-1	1.00	4.53	40.7	7.7	51. 2				957 ± 40	3627 ± 58	150 ± 137	283 ± 28	127 ± 25	232	100.1
VIC1-5-1	A-1	1.00	5.25	40.6	7.9	51. 1	97 ± 18			1310 ± 52	3573 ± 86		333 ± 59	60 ± 53	231	100.2
VIC1-6-1	A-1	1.00	1.04	40.6	7.2	51. 5				1027 ± 33	3680 ± 66		317 ± 59		60	99.8
VIC1-6-2	A-1	1.00	3.99	40.7	7.8	50. 8	137 ± 64			1030 ± 35	3780 ± 39	130 ± 17	310 ± 28		147	99.8

H_2O concentrations are calculated using (2), see text for details. Analytical errors represent larger standard deviation calculated from either at least three probe analyses or microprobe counting statistics. The data are confined to olivine grains polished parallel to [010].

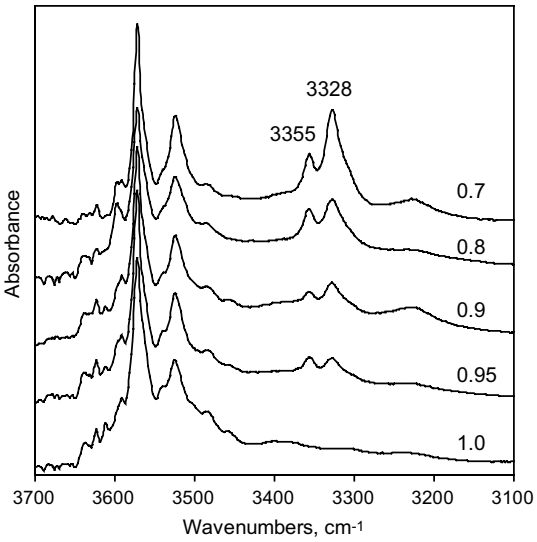

Fig. 7. Examples of FTIR spectra with decreasing (top to bottom) intensities of Group 2 OH IR absorption bands. $A_{\text{net ratio}}$ values are shown above each spectrum. Intensities of the 3572 cm^{-1} absorption peak are reduced to approximately similar values for easy comparison and spectra are stacked for clarity.

diamond-bearing peridotites (Matveev et al., 2006). Such a variety of fO_2 conditions suggests that hydrous defects in natural olivine are associated not only with Fe^{3+}, but also with other tri-valent cations (Berry et al., 2007; Grant et al., 2007b). Thus, the intensity of Group 2 bands likely cannot be developed into a reliable oxy-barometer. In particular, for olivines crystallizing at hydrous conditions hydrogen defects are associated with various tri-valent cations and therefore cannot be directly related to increasing $Fe^{3+}$with increasing fO_2. This is consistent with experimental results of Matveev et al. (2001) and Berry et al. (2007) suggesting that although increasing fO_2 may promote the formation of Group 2 bands, these bands cannot be a product of oxidation alone as experimentally annealed natural olivines show Group 2 OH IR absorption bands only at high $aSiO_2$.

It appears that high $aSiO_2$ is a necessary but not the only requirement for the formation of hydrous defects associated with Group 2 bands. This may explain that in some experimental studies Group 2 bands were not formed even though $aSiO_2$ was buffered at the olivine–orthopyroxene equilibrium (see above). Many olivines coexisting with orthopyroxene in peridotitic nodules also show Group 1 rather than Group 2 OH absorption bands (e.g. Miller et al., 1987; Matsyuk and Langer, 2004; Peslier and Luhr, 2006; Grant et al., 2007a). This observation may relate to disequilibrium though, with lower $aSiO_2$ imposed on olivine during upward transport in opx-undersaturated melts (e.g. kimberlite) or during mantle metasomatism (Wallace and Green, 1988; Green and Wallace, 1988; Matveev et al., 2001 and references therein). The stability of hydrous defects associated with Group 2 OH bands may also be affected by the trace element composition of olivine: For example, Ti-doped natural olivines develop Ti-clinohumite-type hydrous defects (Group 1) rather than defects associated with tri-valent cations (Group 2) (Berry et al., 2007). In addition, possible fO_2 effects have to be considered (see above) and, therefore, absence of Group 2 bands in olivine may not necessarily be indicative of lower $aSiO_2$. In view of the available experimental data we conclude that the presence of these bands is, however, indicative of high $aSiO_2$ conditions.

The relative intensity of Group 2 bands may be expressed as ratio of the net linear absorbencies of the major peaks of Groups 1 and 2 (3572 and 3328 cm^{-1}, respectively; see Fig. 5):

$$A_{\text{net ratio}} = A_{\text{net}(3572)}/(A_{\text{net}(3572)} + A_{\text{net}(3328)}) \quad (4)$$

Olivines with $A_{\text{net ratios}}$ below 1 (i.e. with a contribution of Group 2 bands) are not expected to have been in equilibrium with kimberlitic melts, because of the inferred association of Group 2 absorbance bands with higher $aSiO_2$ (hyperstene-normative melts). Kimberlite hosted olivines with Group 2 bands probably represent xenocrysts from lherzolitic or harzburgitic sources and are reminiscent of structural equilibration with orthopyroxene in these rocks during mantle residence (Matveev et al., 2001). Consequently, for peridotitic olivines, the $A_{\text{net ratio}}$ may be interpreted as an indicator for the degree of re-equilibration with kimberlitic melts and may correlate with the residence time in ascending magmas. Interaction of peridotitic olivines with hydrous, low $aSiO_2$ kimberlitic melts during sampling and ascent will result in increasing water concentrations and in particular in increasing Group 1 bands. However, if this interaction is short, e.g. only during rapid ascent from the point of entrainment or xenolith disaggregation, olivine spectra would retain the features typical of derivation from anhydrous, orthopyroxene-bearing depleted mantle. Accordingly, olivines from diamond-bearing peridotitic xenoliths show primarily Group 2 OH absorption bands and are depleted in H_2O (Matveev et al., 2006).

Another possibility is that the dramatic increase in $aSiO_2$ reflected by spectra with $A_{\text{net ratio}} < 1$ is a result of contamination of the kimberlitic melt with silica-rich crustal material at or above the Moho. Lack of direct evidence for such a process, other than olivine phenocrysts with $A_{\text{net ratio}} < 1$, suggests that crustal contamination during ascent is likely spatially limited and short lived, with the produced silica enriched liquids subsequently being mixed back into much larger volumes of uncontaminated low $aSiO_2$ kimberlitic magma.

4.1.3. Group 3 spectra and the broad OH absorption band at 3220 cm^{-1}

This absorption band has a FWHM (Full Width at Half Maximum) of ~50 cm^{-1}, which is broader than any other OH absorption band commonly observed in kimberlitic olivines. The band was observed in at least half of the studied kimberlite derived olivines, either alone or in association with absorption Group 1, or Group 2 or both. However, only in 30% of the spectra the absorption peak was well developed.

The origin of this band is poorly understood. A similar broad band, located at 3160 cm^{-1}, was observed in spectra

of pure forsterite experimentally equilibrated with orthopyroxene at high pressure. It was proposed that this band, similar to Group 2 bands, is characteristic of high $aSiO_2$ conditions and corresponds to hydrous defects associated with Mg vacancies (Lemaire et al., 2004; Berry et al., 2007) or their clusters (Keppler and Bolfan-Casanova, 2006). The proximity in FTIR spectra combined with a similarly broad width may suggest that the bands at 3160 and 3220 cm^{-1} measured in synthetic and natural olivines, respectively, could have a similar origin. In this case, the presence of the 3220 cm^{-1} band in spectra of kimberlitic olivines could also be associated with clustered Mg vacancies and thus be indicative of increased $aSiO_2$. However, there are arguments against a common origin of the low frequency bands in pure forsterite and natural Fe-bearing olivine: in the olivine structure Ti charge compensates Mg vacancies and thus causes the band at 3160 cm^{-1} to disappear from the spectrum of synthetic forsterite (Berry et al., 2007; Keppler and Bolfan-Casanova, 2006). At the same time, for natural olivines Ti does not seem to significantly affect the intensity of the 3220 cm^{-1} band: the band was observed in the spectra of olivine D2-7, having the highest TiO_2 content (308 ppm) of all studied samples, and of olivine VIC1-6-1 in which Ti is below the detection limit (Table 2). The band at 3220 cm^{-1} was not observed in the spectra of basaltic phenocrysts regardless of $aSiO_2$ (Matveev et al., 2005). In kimberlitic olivines this band may occur together with any combination of bands: Group1 A, B, C and Group 2. This suggests that the only parameter that controls the occurrence of this band is elevated water or hydrogen fugacity. Thus this band could be associated with the presence of either humite-type defects (Matsyuk and Langer, 2004; Mosenfelder et al., 2006) or isolated hydroxyl groups, which are predicted by computer simulations (Braithwaite et al., 2003).

4.2. Hydroxyl concentrations in kimberlitic olivines

Water concentrations in kimberlitic olivines range from below the limit of detection for our FTIR setup (i.e. <1 ppm) to 365 ppm (Table 2). The relative proportion of hydroxyl-rich and hydroxyl-poor olivines varies from kimberlite to kimberlite. At the same time, combining the H_2O concentrations for all the studied grains results in a near normal distribution with a mean value at ~150 ppm and $1\sigma = 74$ ppm (Fig. 8).

A comparison of measured water concentrations with experimental data from Kohlstedt et al. (1996) and Matveev et al. (2001) allows estimating the minimum pressure of olivine crystallization/hydrogenation. The mean water concentration of 150 ppm corresponds to a minimum pressure of olivine crystallization or hydrogenation of ~0.7 GPa (Fig. 8). Olivines with the highest measured H_2O concentration (365 ppm) would equilibrate experimentally with a pure aqueous fluid at 1.5 GPa. However, if hydrogenation of olivine occurred during interaction with a hydrous kimberlitic melt, real pressures of hydrogenation would be significantly higher than the above minimum estimates based on interaction with a hydrous fluid. According to various estimates, the molar concentration of water (X_{H_2O}) in kimberlitic melts varies between 0.14 and 0.30

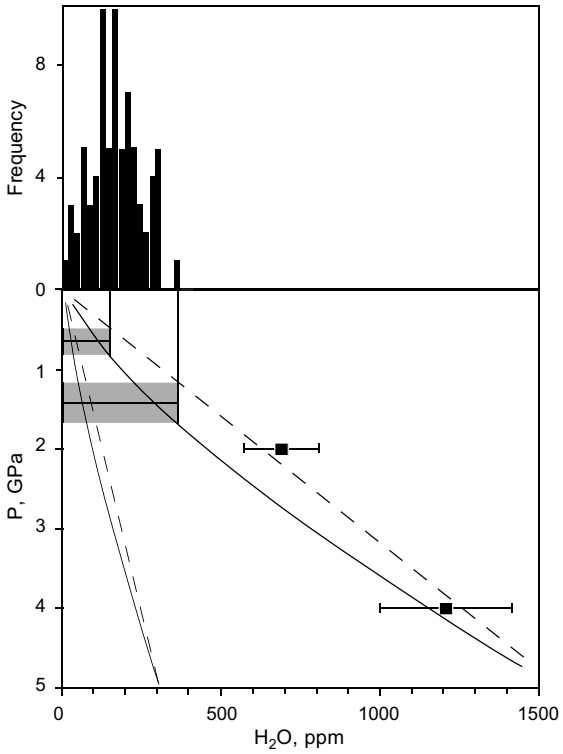

Fig. 8. Comparison of water concentrations measured in kimberlitic olivines (histogram, top) with experimental data (bottom). Filled squares with error bars are calculated from FTIR spectra of magnesiowüstite-buffered olivines (Matveev et al., 2001) using expression (2). The bold solid curve (right side of bottom diagram: ($X_{H_2O} = 1$) represents a regression from Kohlstedt et al. (1996) multiplied by the calibration adjustment factor of 3.5 of Bell et al. (2003a); the associated dashed line is a regression through the origin for recalculated data points from Matveev et al. (2001). The solid and dashed curves on the left (low H_2O) side of the diagram represent the estimated H_2O contents for olivines (recalculated after Kohlstedt 1996 and Matveev et al., 2001, respectively) in equilibrium with a hydrous ($X_{H_2O} = 0.2$) kimberlitic melt. The diagram allows to estimate the minimum pressure of hydrogenation (olivine equilibrium with aqueous fluid) and the pressure at which olivine equilibrates with a hydrous melt.

(Price et al., 2000; Le Roex et al., 2003; Harris et al., 2004). The estimated water solubility in olivine in equilibrium with kimberlitic melt with $X_{H_2O} \sim 0.2$ is shown in Fig. 8. The estimate is relatively rough since it does not take into account the solubilities of (Fe, Mg)O and SiO_2 in the experimental fluids, as well as the activity coefficients of water in both experimental fluids and kimberlitic melts. Nevertheless, the estimate is probably accurate enough to predict that olivine with water contents of 150 ppm (mean value) to 365 ppm (max. value) would have been in equilibrium with a kimberlitic melt at pressures exceeding 2.5 and 5 GPa, respectively. These minimum equilibration pressures would increase further if hydrogen loss during magma ascent occurred. Hydrogen loss from kimberlitic olivines is not expected to be significant through, owing to very rapid ascent of kimberlitic magmas (Canil and Fedortchouk, 1999; Kelley and Wartho, 2000; Bell et al., 2003b; Peslier and Luhr, 2006).

4.3. Olivine chemical compositions and their interpretation

The chemical composition of the studied olivines is reported in Table 2 and Figs. 9 and 10. The forsterite content (Mg#) of the analyzed olivines varies from 88 to 94 (Fig. 9a). The majority of high-Mg olivines (Mg# > 90) also have high NiO contents (>3500 ppm). Such chemical compositions are characteristic of peridotitic olivines from depleted lithospheric mantle (Griffin et al., 1989). In less magnesian olivines, MnO systematically increases and NiO systematically decreases with decreasing forsterite content. Such compositional trends reflect evolution of the host kimberlitic melt resulting from olivine crystallization, i.e. magmatic differentiation (Fig. 9a and b). Accordingly, olivines with less than 3300 ppm NiO represent phenocrysts crystallized from somewhat evolved kimberlitic melt.

Regardless of the source kimberlite, olivine phenocrysts with NiO < 3300 ppm have high and near constant TiO_2 contents of ~280 ppm (Fig. 9c). Olivine phenocrysts also contain uniform (within analytical error) CaO contents of ~310 ppm (Fig. 9d). The anomalously Ca-rich olivines from FALC are considered to represent xenocrysts.

Water concentrations can be used to separate olivine phenocrysts into high-H_2O (250 ± 50 ppm) and low-H_2O (100 ± 40 ppm) groups (Fig. 9e). Crystallization of H_2O-free phenocrysts should occur during the final stages of kimberlite emplacement but because of their small size such micro-phenocrysts and groundmass crystals were not studied here.

Comparing the major and trace element composition of olivine (phenocrystic and xenocrystic) with its water concentration did not reveal any straightforward correlations. This lack of correlations is not surprising considering the variety of mechanisms for the stabilization of hydrous defects and the diverse conditions of crystallization (Berry et al., 2007; Demouchy and Mackwell, 2006; Grant et al., 2007a,b). In addition, in many of the studied olivine grains trace element concentrations are close to detection limits of

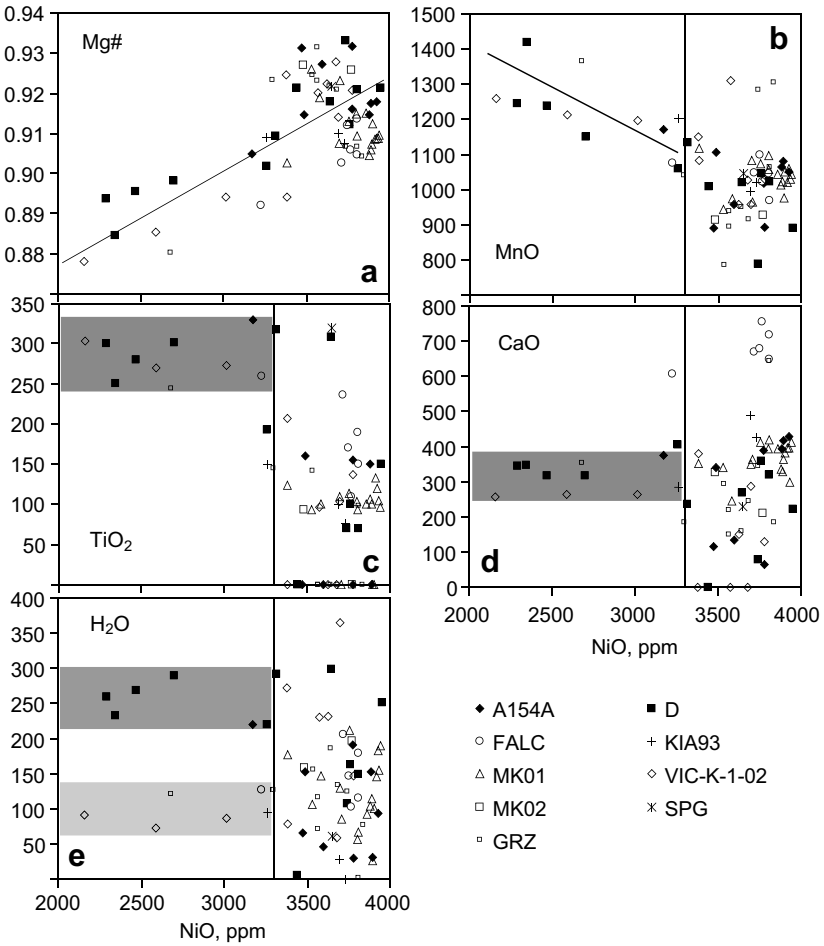

Fig. 9. Composition of kimberlitic olivines. Concentrations of Mg#, MnO, TiO_2, CaO and H_2O versus NiO content of kimberlite derived olivines. Olivines with NiO contents below 3300 ppm are magmatic phenocrysts; for higher NiO contents both a pheno- and a xenocrystic origin are possible. (a) Decreasing NiO with decreasing forsterite content and (b) negative correlation of NiO and MnO are indicative of magmatic fractionation; (c) phenocrystic olivines contain high and uniform concentrations of $TiO_2 \sim 280 \pm 50$ ppm; (d) the CaO concentration of kimberlitic phenocrysts remains constant within analytical error at $\sim 310 \pm 50$ ppm. Xenocrysts from FALC contain anomalously high CaO concentrations >600 ppm and (e) phenocrysts can be divided into high-H_2O olivines, likely in equilibrium with an aqueous fluid, and low-H_2O olivines, in equilibrium with kimberlitic melt.

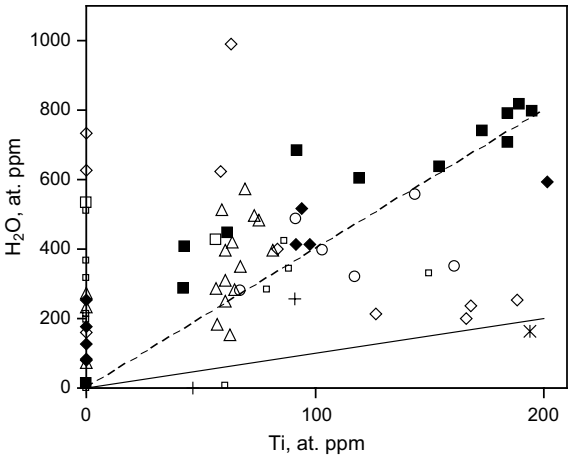

Fig. 10. Relative molar proportion of Ti and H_2O in kimberlitic olivines. The solid line represents a 1:1 molar proportion of Ti to H_2O which according to Berry et al. (2005) outlines the maximum amount of water that could be associated with Ti in hydrous defects. The dashed line is a regression through the origin for olivines from A154-S and corresponds to a molar H_2O:$TiO_2$of 4:1. The observed significant excess of H_2O over Ti illustrates that Ti generally does not control the incorporation of H in the crystal structure of kimberlitic olivines. For legend see Fig. 9.

microprobe analyses (Table 2). However, a recent study particularly emphasized the significance of Ti in the stabilization of the hydrous defects in olivine at shallow mantle conditions (Berry et al., 2007). A possible control of Ti on OH substitution in kimberlitic olivines may be tested by plotting the molar proportions of Ti versus the molar proportion of water (Fig. 10). Following the model of Berry et al. (2007), for each mole of Ti olivine is capable of dissolving up to 1 mole of H_2O. Our calculations result in water concentrations significantly exceeding this proportion (Fig. 10). Molar H_2O–Ti ratios >1 are not restricted to olivines crystallized at high pressures in stability field of garnet peridotite (Group 1A OH absorption bands), but are also observed for olivines crystallizing at shallower conditions (Group 1B and C OH absorption bands) in which hydrous defects associated with Ti should dominate (Berry et al., 2007). It would thus appear that Ti-related hydrous defects are less significant in the structure of kimberlitic olivines than anticipated from experimental results.

Ti in kimberlitic olivine may be coupled with OH in some cases and decoupled in others. A possible correlation of Ti and H_2O is observed for olivines from the A154-S kimberlite (Fig. 10). However, the water concentration in these olivines is four times higher than the capacity of Ti-related hydrous defects. This rather suggests that this correlation is due to a similar geochemical behaviour of water and Ti during evolution of the kimberlite magma at A154-S, the only sample location where this trend was observed.

Considering olivine phenocrysts only, Ti can still clearly be shown to be decoupled from water. Ti contents of phenocrystic olivines are invariably high (250–340 ppm), irrespective of water content (cf. Fig. 9c and e).

Based on the intensity and position of the IR OH absorption bands we define three types of phenocrysts: (i) high H_2O, moderate crystallization pressures (1–2 GPa; Group 1B); (ii) low H_2O, high crystallization pressures (>2 GPa; Group 1A) and (iii) low H_2O, low crystallization pressures (<1 GPa, Group 1C). All of the olivine phenocrysts from A154-S contain relatively high and uniform water concentrations of ~250 ppm (Fig. 9e). Such uniformity is remarkable considering that the water content in xenocrystic olivines from A154-S ranges from 5 to 300 ppm. Based on water absorption bands, the olivine phenocrysts fall into Group 1B suggesting only moderate pressures of crystallization (<2 GPa, see Section 4.1.1). The combination of moderate crystallization pressures and relatively high water contents implies that water fugacity during olivine crystallization or equilibration likely was defined by an aqueous fluid rather than a melt (Fig. 8). The estimated pressure of crystallization based on water contents of A154-S olivines roughly coincides with the depth of the Moho, located at 35–45 km depth beneath the North American craton (Nitescu et al., 2003; Snyder et al., 2004; Németh et al., 2005). We speculate that kimberlitic magmas may sometimes become stagnant at depth of the Moho due to abrupt changes in rheology and density at the crust–mantle boundary. In such a scenario, interaction with crustal rocks may increase the silica content of the melts sufficiently to trigger exsolution of an aqueous fluid (Keppler, 2003). The exsolved fluid may subsequently assist in further magma ascent trough the crust.

Clearly, olivine crystallization can also occur in a more typical environment, i.e. during uninterrupted ascent of kimberlitic magma from the deep mantle. Olivine phenocrysts from the Grizzly and Victor kimberlites contain only ~120 ppm of water and classification of FTIR spectra as Group 1A is suggestive of relatively high crystallization pressures (>2 GPa). Here, water fugacity was controlled by the kimberlitic melt and there are no indications for the exsolution of an aqueous fluid.

One olivine phenocryst from the Victor kimberlite has an unusually high $A_{\text{net ratio}}$ of 0.7 and a relatively low water content of ~90 ppm. Group 1C IR OH absorption bands suggest crystallization at low pressure (<1 GPa). This kimberlitic phenocryst could have crystallized at relatively high $aSiO_2$, resulting from assimilation of siliceous rocks in the upper continental crust.

4.4. Application to kimberlite exploration

The current study clearly establishes that high water content is the primary characteristic to identify kimberlitic olivines in mineral concentrates, e.g. derived from till samples. Over 80% of the studied kimberlitic olivines contain >100 ppm of structural water (Fig. 8, Table 2). For comparison, olivine phenocrysts from hydrous basaltic lavas contain <25 ppm H_2O (recalculated from Matveev et al., 2005). The highest water concentration reported for peridotitic olivines is 45 ppm (Demouchy et al., 2006). Differences in the water contents of olivines from different sources relate to hydrogenation at different water fugacities (mainly pressure and water content) and subsequent hydrogen loss (Demouchy et al., 2006; Peslier et al., 2006; Peslier and Luhr, 2006).

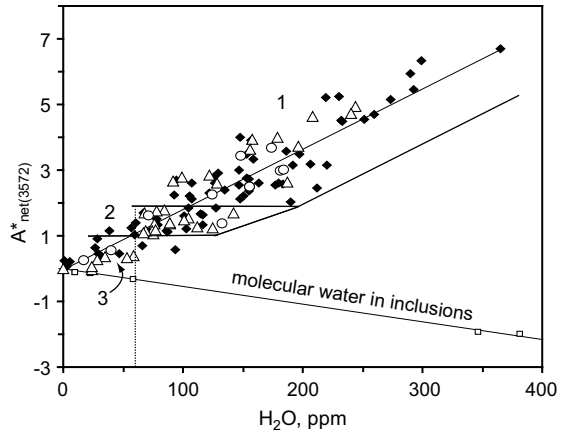

Fig. 11. Primary characteristics that allow reliably identifying kimberlitic olivines are high H_2O concentrations and high intensities of the OH absorption band at 3572 cm^{-1}. Filled symbols are data obtained for polished samples (Table 2). Open symbols represent unpolished olivines from additional kimberlite (triangles) and till samples (circles). Field 1 contains samples for which a kimberlitic origin can be confirmed with high confidence, samples in Field 2 are of likely kimberlitic origin. Based on FTIR data, olivines from Field 3 cannot be confidently identified as being kimberlitic. Olivines crystallized from various basaltic and alkali basaltic melts will fall into Field 3. Olivines with elevated water contents due to fluid inclusions or to incipient alteration also have negative $A^*_{net(3572)}$ as indicated by four samples shown as open squares.

A potential problem in employing water content as the principal criterion to distinguish kimberlitic from non-kimberlitic olivines is the possibility of high molecular water in olivine associated with fluid inclusions or of hydrous alteration (e.g. during serpentinization). Hence, we introduce a second test parameter ($A^*_{net(3572)}$) based on the observation that all water-rich kimberlitic olivines show a strong absorption peak at 3572 cm^{-1}. Our test parameter for structural versus molecular water/alteration is defined as the difference in absorbance measured at 3572 cm^{-1} (i.e. the main Group 1 peak) and at 3425 cm^{-1} (i.e. the trough dividing Group 1 and 2 OH absorption bands, see Fig. 5). Normalized to 1 cm sample thickness, $A^*_{net(3572)}$ denotes the net intensity of the absorption peak at 3572 cm^{-1} and is calculated as follows:

$$A^*_{net(3572)} = ((A_{(3572)} - A_{(3425)})^*6366)/A_{int,\ Si\text{–}O\ overtone} \quad (5)$$

Here, OH absorbencies (A) include a background correction fixed at 3130 and 3755 cm^{-1}. The coefficient 6366 and the integrated absorbance of the 2nd order Si–O overtone ($A_{int,\ Si\text{–}O\ overtone}$), for normalization to 1 cm sample thickness are from Eq. (1).

Based on this definition, $A^*_{net(3572)}$ delivers information on the nature of elevated water concentrations in olivine. For kimberlite indicators, elevated water concentrations are present as structurally bonded OH and, therefore, $A^*_{net(3572)}$ will have positive values and correlate positively with water content (Fig. 11). Molecular water, however, forms a single, very broad absorption band covering the entire OH absorption region with a maximum located at ~3300 cm^{-1}. Consequently, if molecular water is present, then $A_{(3572)} < A_{(3425)}$, and $A^*_{net(3572)}$ is negative. Hydrous products of olivine alteration (e.g. chlorite, serpentine, talk) absorb IR radiation at higher wavenumbers (~3700 cm^{-1}) than olivine (Miller et al., 1987; Matsyuk and Langer, 2004). If elevated water concentrations are caused by alteration and olivine does not contain structurally bonded OH, $A^*_{net(3572)}$ will be close to zero. Consequently, all water-bearing olivines with $A^*_{net(3572)} \leqslant 0$ are not useful as kimberlite indicators.

Fig. 11 shows data measured on the polished olivines listed in Table 2 and also on rough (unpolished) olivine grains collected from a range of kimberlites and till samples. All FTIR spectra were processed using the algorithm proposed here implemented as macro. Water concentrations were calculated using (2), $A^*_{net(3572)}$ using (5).

The probability of olivine being of kimberlitic origin increases with increasing H_2O content and $A^*_{net(3572)}$. Fig. 11 can thus be divided into three fields corresponding to different confidence levels for an assigned kimberlitic origin. To define these fields we assume that, based on literature data, the occurrence of non-kimberlitic olivines with a water content >60 ppm is extremely unlikely (e.g. Matveev et al., 2005; Demouchy et al., 2006; Peslier and Luhr, 2006). Considering the spread of data points along the regression line (Fig. 11), this cut-off at 60 ppm water corresponds to a maximum $A^*_{net(3572)} = 1.9$ and this value outlines "Field 1", i.e. "high confidence" kimberlitic olivines. The cut-off for "Field 2" corresponds to an average $A^*_{net(3572)} = 1$ at 60 ppm of water, and this field contains olivines of "likely" kimberlitic origin. "Field 3" includes samples for which a kimberlitic origin cannot be confirmed using FTIR spectroscopy.

Data measured on polished and rough olivine grains follow the same trend of increasing water content and $A^*_{net(3572)}$ and hence, Fig. 11 can be used to confidently identify kimberlitic olivines without a necessity for sample preparation. Best results are achieved for unaltered grains free of fluid, melt or mineral inclusions. However, even optically imperfect grains often produce useful spectra.

5. CONCLUSIONS

In the present study we developed a technique to unambiguously identify kimberlitic olivines in mineral concentrates (where olivine is particularly common in artic climates) based on FTIR spectroscopy. The technique is simple to use, robust—sample preparation is not necessary and micro-FTIR spectra may be acquired from unpolished grains—and data processing and evaluation may largely be automated in the form of macros.

The developed spectral classification describes OH IR absorption in olivine using three major characteristics: (1) the type of Group 1 OH IR absorption bands (Type A, B or C, indicative of the pressure of hydrogenation); (2) the relative proportion of Group 2 OH IR absorption bands (allowing to make inferences on aSiO_2) and (3) the absolute concentration of water (with $H_2O > 60$ ppm indicating a kimberlitic origin). Olivines with high water contents and

strong Group 1 OH IR absorption bands are very good kimberlite indicators for exploration purposes.

Our straightforward classification of olivine FTIR spectra allows rapid processing of a statistically significant number of olivine grains per sample. In addition, a characterization of kimberlite occurrences using FTIR spectra of olivine will help to gain insights into kimberlite ascent rates and possible storage in intermediate magma reservoirs.

ACKNOWLEDGMENTS

The authors thank Bruce Wyatt and Faye Logan (De Beers Canada) for samples and De Beers Canada for financial support. Bruce G. Kienlen (Diamonds North Resources Ltd.) supplied unpolished samples used during testing of the method. Don Resultay and Mark Labbe for expertly crafted polished samples of olivine. George Rossman, Sylvie Demouchy and an anonymous reviewer are thanked for constructive comments that helped to significantly improve the manuscript. T.S. acknowledges funding through an NSERC Discovery grant and the CRC program.

REFERENCES

Armstrong J. T. (1995) A package of correction programs for the quantitative electron microbeam X-ray analysis of thick polished materials, thin films, and particles. *Microbeam Anal.* **4**, 177–200.

Bai Q. and Kohlstedt D. L. (1993) Effects of chemical environment on the solubility and incorporation mechanism for hydrogen in olivine. *Phys. Chem. Miner.* **19**, 460–471.

Bell D. R., Ihinger P. D. and Rossman G. R. (1995) Quantitative analysis of trace OH in garnet and pyroxenes. *Amer. Mineral.* **80**, 465–474.

Bell D. R., Rossman G. R., Maldener J., Endlisch D. and Rauch F. (2003a) Hydroxide in olivine: a quantitative determination of the absolute amount and calibration of the IR spectrum. *J. Geophys. Res.* **108**(B2), ECV8-1–ECV8-9.

Bell D. R., Rossman G. R. and Moore R. O. (2003b) Abundance and partitioning of OH in a high pressure magmatic system: megacrysts from the Monastery kimberlite, South Africa. *J. Petrol.* **45**(8), 1539–1564.

Berry A., Hermann J., O'Neill H. S. C. and Foran G. J. (2005) Fingerprinting the water site in mantle olivine. *Geology* **33**(11), 869–872.

Berry A. J., O'Neill H. S. C., Hermann J. and Scott D. R. (2007) The infrared signature of water associated with trivalent cations in olivine. *Earth Planet. Sci. Lett.* **261**, 134–142.

Berryman A. K., Scott Smith B. H. and Jellicoe B. C. (2004) Geology and diamond distribution of the 140/141 kimberlite, Fort à la Corne, central Saskatchewan, Canada. *Lithos* **76**, 99–114.

Braithwaite J. S., Wright K. and Catlow C. R. A. (2003) A theoretical study of the energetics and IR frequencies of hydroxyl defects in forsterite. *J. Geophys. Res.* **108**, ECV 1–ECV 9.

Brian D. and Bonner R. (2003) The Diavik diamond mine, Lac de Gras, Northwest Territories, Canada. In: *VIIIth International Kimberlite Conference, Slave Province and Northern Alberta Field Trip Guidebook* (ed. B. A. Kjarsgaard), pp. 61–65.

Canil D. and Fedortchouk Y. (1999) Garnet dissolution and the emplacement of kimberlites. *Earth Planet. Sci. Lett.* **167**(3–4), 227–237.

Canil D., Schulze D. J., Hall D., Hearn, Jr., B. C. and Milliken S. M. (2003) Lithospheric roots beneath western Laurentia: the geochemical signal in mantle garnets. *Can. J. Earth Sci.*(40), 1027–1051.

Chiarenzelli J. R., Aspler L. B. and Villeneuve M. (1996) Characterisation, origin and paleaproterozoic history of the Saskatchewan Craton and possible implications for Trans-Hudson Orogen. Lithoprobe Trans-Hudson Orogen Transect. In *Report of VIth Transect Meeting*, vol. 55, University of Saskatchewan, pp. 26–38.

Davis W. J. and Kjarsgaard B. A. (1997) A Rb–Sr isochron age for a kimberlite from the recently discovered Lac de Gras Field, Slave Province, Northwest Canada. *J. Geol.* **105**, 503–509.

Demouchy S. and Mackwell S. (2006) Mechanisms of hydrogen incorporation and diffusion in iron-bearing olivine. *Phys. Chem. Miner.* **33**(5), 347–355.

Demouchy S., Jacobsen S. D., Gaillard F. and Stern C. R. (2006) Rapid magma ascent recorded by water diffusion profiles in mantle olivine. *Geology* **34**(6), 429–432.

Field M. and Scott Smith B. H. (1999) Contrasting geology and near surface emplacement of kimberlite pipes in Southern Africa and Canada. *VIIth International Kimberlite Conference*, 214–237.

Fipke C. E., Dummett H. T., Moore R. O., Carlson J. A., Ashley R. A., Gurney J. J. and Kirkley M. B. (1995) History of the discovery of diamondiferous kimberlites in the Northwest Territories, Canada. *VIth International Kimberlite Conference*, 158–160.

Graham I., Burgess J., Bryan D., Ravenscroft P. J., Thomas E., Doyle B. J., Hopkins R. and Armstrong K. A. (1999) Exploration history and geology of the Diavik kimberlites, Lac de Gras, Nothwest Territories, Canada. *VIIth International Kimberlite Conference*, 262–279.

Grant K., Ingrin J., Lorand J. and Dumas P. (2007a) Water partitioning between mantle minerals from peridotite xenoliths. *Contrib. Mineral. Petrol.* **154**(1), 15–34.

Grant K. J., Kohn S. C. and Brooker R. A. (2007b) The partitioning of water between olivine, orthopyroxene and melt synthesised in the system Albite–Forsterite–H_2O. *Earth Planet. Sci. Lett* **260**(1–2), 227–241.

Green D. H. and Wallace M. E. (1988) Mantle metasomatism by ephemeral carbonatite melts. *Nature* **336**, 459–462.

Griffin W. L., Cousens D. R., Ryan C. G., Sie S. H. and Suter G. F. (1989) Ni in chrome pyrope garnets: a new geothermometer. *Contrib. Mineral. Petrol.* **103**, 199–202.

Harris M., Le Roex A. and Class C. (2004) Geochemistry of the Uintjiesberg kimberlite, South Africa: petrogenesis of an off-craton, group I, kimberlite. *Lithos* **74**(3–4), 149–165.

Heaman L. M., Kjarsgaard B. A. and Creaser R. A. (2004) The temporal evolution of North American kimberlites. *Lithos* **76**, 377–397.

Jamtveit B., Brooker R., Brooks K., Larsen L. M. and Pedersen T. (2001) The water content of olivines from the North Atlantic Volcanic Province. *Earth Planet. Sci. Lett.* **186**(5772), 401–415.

Jarosewich E. (2002) Smithsonian Microbeam Standards. *J. Res. Natl. Inst. Stand. Tech.* **107**(6), 681–685.

Karner J., Papike J. J. and Shearer C. K. (2003) Olivine from planetary basalts; chemical signatures that indicate planetary parentage and those that record igneous setting and process. *Amer. Mineral.* **88**, 806–816.

Kelley S. P. and Wartho J. A. (2000) Rapid kimberlite ascent and the significance of Ar–Ar ages in xenolith phlogopites. *Science* **289**(5479), 609–611.

Keppler H. (2003) Water solubility in carbonatite melts. *Amer. Mineral.* **88**, 1822–1824.

Keppler H. and Bolfan-Casanova N. (2006) Thermodynamics of water solubility and partitioning. *Rev. Mineral. Geochem.* **62**, 193–230.

Köhler T. P. and Brey G. P. (1990) Calcium exchange between olivine and clinopyroxene calibrated as a geothermobarometer for natural peridotites from 2 to 60 kb with applications. *Geochim. Cosmochim. Acta* **54**, 2375–2388.

Kohlstedt D. L. and Mackwell S. J. (1998) Diffusion of hydrogen and intrinsic point defects in olivine. *Z. Phys. Chem.* **207**, 147–162.

Kohlstedt D. L., Keppler H. and Rubie D. C. (1996) Solubility of water in the α, β and γ phases of $(Mg,Fe)_2SiO_4$. *Contrib. Mineral. Petrol.* **123**(4), 345–357.

Lemaire C., Kohn S. C. and Brooker R. A. (2004) The effect of silica activity on the incorporation mechanisms of water in synthetic forsterite: a polarised infrared spectroscopic study. *Contrib. Mineral. Petrol.* **147**(1), 48–57.

Le Roex A. P., Bell D. R. and Davis P. (2003) Petrogenesis of group I kimberlites from Kimberley, South Africa: evidence from bulk-rock geochemistry. *J. Petrol.* **44**(12), 2261–2286.

Lewry J. F., Hajnal Z., Green A., Lucas S. B., White D., Stauffer M. R., Ashton K. E., Weber W. and Clowes R. (1994) Structure of a Paleoproterozoic continent-continent collision zone: a LITHOPROBE seismic reflection profile across the Trans Hudson Orogen, Canada. *Tectonophysics* **232**, 143–160.

Libowitzky E. and Rossman G. R. (1996) Principles of quantitative absorbance measurements in anisotropic crystals. *Phys. Chem. Miner.* **23**, 319–327.

Libowitzky E. and Rossman G. R. (1997) An IR absorption calibration for water in minerals. *Amer. Mineral.* **82**, 1111–1115.

Mackwell S. J. and Kohlstedt D. L. (1990) Diffusion of hydrogen in olivine: implications for water in the mantle. *J. Geophys.Res.* **95**, 5079–5088.

Matsyuk S. S. and Langer K. (2004) Hydroxyl in olivines from mantle xenoliths in kimberlites of the Siberian platform. *Contrib. Mineral. Petrol.* **147**, 413–437.

Matveev, S. (1997) CHO fluids at upper mantle conditions. Ph.D. thesis, Universität zu Köln, Germany.

Matveev S., O'Neill H. S. C., Ballhaus C., Taylor W. R. and Green D. H. (2001) Effect of silica activity on OH^- IR spectra of olivine: implications for low-aSiO_2 mantle metasomatism. *J. Petrol.* **42**(4), 721–729.

Matveev S., Portnyagin M., Ballhaus C., Brooker R. and Geiger C. A. (2005) FTIR spectrum of phenocryst olivine as an indicator of silica saturation in magmas. *J. Petrol.* **46**, 603–614.

Matveev S., Creighton S. and Stachel T. (2006) OH in peridotitic olivines entrained in kimberlitic magma. *Sixteenth annual V.M. Goldschmidt International Conference*, Melbourne (abstr.).

Miller G. H., Rossman G. R. and Harlow G. E. (1987) The natural occurrence of hydroxide in olivine. *Phys. Chem. Miner.* **14**, 461–472.

Mitchell R. H. (1986) *Kimberlites: Mineralogy, Geochemistry, and Petrology*. Plenum Press, New York, p. 442.

Mosenfelder J. L., Deligne N. I., Asimow P. D. and Rossman G. R. (2006) Hydrogen incorporation in olivine from 2–12 GPa. *Amer. Mineral.* **91**, 285–294.

Németh B., Clowes R. M. and Hajnal Z. (2005) Lithospheric structure of the Trans-Hudson Orogen from seismic refraction—wide-angle reflection studies. *Can. J. Earth Sci. (Rev. Can. Sci. Terre)* **42**(4), 435–456.

Nitescu B., Cruden A. R. and Bailey R. C. (2003) Topography of the crust–mantle interface under the Western Superior craton from gravity data. *Can. J. Earth Sci.*, 1307–1320.

Nowicki T., Crawford B., Dyck D., Carlson J., McElroy R., Oshust P. and Helmstaedt H. (2004) The geology of kimberlite pipes of the Ekati property, Northwest Territories, Canada. *Lithos* **76**, 1–27.

Paterson M. (1982) The determination of hydroxyl by infrared absorption in quartz, silicate glasses and similar materials. *Bull. Minéral.* **105**, 20–29.

Peslier A. H. and Luhr J. F. (2006) Hydrogen loss from olivines in mantle xenoliths from Simcoe (USA) and Mexico: mafic alkalic magma ascent rates and water budget of the sub-continental lithosphere. *Earth Planet. Sci. Lett.* **242**, 302–319.

Peslier, A., Luhr, J., Woodland, A., Wolff, J., and Meen, J. 2006. Estimating alkali basalt and kimberlite magma ascent rates using H diffusion profiles in xenolithic mantle olivine. *Sixteenth annual V.M. Goldschmidt International Conference*, Melbourne (abstr.).

Portnyagin M. V. (1998) Origin of mantle derived magmas in supra-subduction zones: a case study of the Troodos Ophiolite (Cyprus). Ph. D. thesis, Vernadski Institute, Moscow, Russia.

Price S. E., Russell J. K. and Kopylova M. G. (2000) Primitive magma from the Jericho Pipe, NWT, Canada: constraints on primary kimberlite melt chemistry. *J. Petrol.* **41**(6), 789–808.

Scott Smith B. (1996) Kimberlites. In *Undersaturated Alkaline Rocks: Mineralogy, Petrogenesis, and Economic Potential* (ed. R. H. Mitchell). MAC, Short Course Volume, Winnipeg **24**, pp. 217–244.

Skogby H. and Rossman G. R. (1991) The intensity of amphibole OH bands in the infrared absorption spectrum. *Phys. Chem. Miner.* **18**, 64–86.

Smith C. B. (1983) Pb, Sr and Nd isotopic evidence for sources of southern African Cretaceous kimberlites. *Nature* **304**(5921), 51–54.

Smyth J. R., Frost D. J., Nestola F., Holl C. M. and Bromiley G. (2006) Olivine hydration in the deep upper mantle: effects of temperature and silica activity. *Geophys. Res. Lett.* **33**, L15301. doi:10.1029/2006GL026194.

Snyder D. B., Rondenay S., Bostock M. G. and Lockhart G. D. (2004) Mapping the mantle lithosphere for diamond potential using teleseismic methods. *Lithos Selected Papers from the VIIIth International Kimberlite Conference. Volume 2: The J. Barry Hawthorne* **77**(1–4), 859–872.

Wallace M. E. and Green D. H. (1988) An experimental determination of primary carbonatite magma composition. *Nature* **335**, 343–346.

Webb K. J., Scott Smith B. H., Paul J. L. and Hetman C. M. (2004) Geology of the Victor Kimberlite, Attawapiskat, Northern Ontario, Canada: cross-cutting and nested craters. *Lithos* **76**, 29–50.

Zhao Y. H., Ginsberg S. B. and Kohlstedt D. L. (2004) Solubility of hydrogen in olivine: dependence on temperature and iron content. *Contrib. Mineral. Petrol.* **147**(2), 155–161.

Zonneveld J. P., Kjarsgaard B. A., Harvey S. E., Heaman L. M., McNeil D. H. and Marcia K. Y. (2004) Sedimentologic and stratigraphic constraints on emplacement of the Star Kimberlite, east-central Saskatchewan. *Lithos* **76**, 115–138.

Associate editor: J. Kelly Russell